1   **Coupled thermo-hydro-mechanical-chemical modeling of permeability change in porous**

2   **rocks: The significant role of the pressure solution**

3   Hideaki Yasuhara[1], Naoki Kinoshita[1], Sho Ogata[1], Dae-Sung Cheon[2], and Kiyoshi Kishida[3]

4   Department of Civil and Environmental Engineering, Ehime University, Matsuyama, 790-8577,

5   JAPAN.

6   [2] Korea Institute of Geoscience and Mineral Resources, Daejeon, 305-350, KOREA.

7   [3] Department of Urban Management, Kyoto University, Kyoto, 615-8540, JAPAN.

8   *Corresponding Author, hide@cee.ehime-u.ac.jp; Tel&Fax: +81-89-927-9853

9

10 **Abstract**

11   When considering the safe isolation of high-level radioactive wastes, the long-term

12 evolution of the hydraulic and transport behavior of the rocks of interest should be predicted prior

13 to its operation because coupled thermal-hydraulic-mechanical-chemical (THMC) processes

14 should be significantly active in such situations where relatively high ground pressure and

15 temperature are induced. In this study, a coupled THMC numerical model has been developed to

16 examine the long-term change in permeability of the porous sedimentary rocks that are assumed

17 to be composed purely of quartz. Specifically, the chemo-mechanical process of the pressure

18 solution was incorporated into the model. The developed model was validated by replicating the

19 existing experimental measurements of the porosity reduction and the evolving silica

20 concentration. Subsequently, by simulating the burial of high-level radioactive wastes in the deep

21 subsurface, namely, by applying the simulated confining pressure and temperature conditions, the

22 long-term evolution of the rock permeability was predicted. The model predictions clearly

23 showed a significant influence of the pressure dissolution on the change in permeability with time.

24 The predicted permeability of the rocks close to the wastes decreased by one order of magnitude

25 in 10^4 years when considering the pressure dissolution, while the permeability changed little

26 during the same period when the pressure dissolution was not considered. This reduction should

27 delay the dispersion of the radioactive materials dissolved in the groundwater.

28

29

Keywords: Rock permeability, Coupled THMC model, Mineral dissolution, Pressure

solution

32

Highlights:

➢ **A coupled THMC numerical model was developed to predict the long-term change in**

 permeability.

➢ **The developed model considers the pressure solution.**

➢ **The model was validated by replicating the existing experiments.**

➢ **The model enables the long-term evolution of rock permeability to be predicted under**

 arbitrary pressure and temperature conditions.

40

41

1. Introduction

  When disposing high-level radioactive wastes in the deep subsurface, the influence of the

disposal on the hydraulic property of the rocks of interest must be examined in advance and

should be estimated with a certain level of precision. The rocks that work as natural barriers to the

46   migration of radionuclides should be influenced by the convolved phenomena, including the

47   transfer of heat from the wastes, the groundwater flow, the variation in induced stresses, and the

48   geochemical reactions, such as mineral dissolution and precipitation [1], [2]. Therefore, in order

49   to predict the long-term evolution of the hydraulic property, a numerical model that can account

50   for the coupled Thermo-Hydro-Mechanical-Chemical (THMC) processes is required. In particular,

51   the precise modeling of the geochemical reactions, occurring at the interface between the grain

52   particles composing the rocks and the pore water, is of significant importance to achieving precise

53   predictions. To date, THMC numerical models have been developed to address such engineering

54   issues as the geological isolation of CO_2 and radioactive wastes and energy recovery from

55   geothermal reservoirs [3]-[9]. By using some of the above models, the long-term phenomena

56   taking place in the artificial and natural barriers have been predicted by considering the specific

57   geological conditions, the heat transfer, the water flow, the stress/deformation, and the

58   geochemical reactions. In the geochemical calculations of the THMC models, the mineral

59   dissolution and precipitation occurring on the free surfaces of the rocks [10] are typically

60   considered, but the dissolution active at the grain contacts (e.g., pressure dissolution [11]-[18]) is

61   not taken into account. In the literature, it is indicated that the pressure dissolution may change the

62   hydraulic property over a long duration; and therefore, the phenomenon must be incorporated into

63   the modeling process when evaluating the long-term integrity of the rocks in terms of the

64   hydraulic property. Recently, several THMC numerical models that can consider the process of

65   the pressure dissolution have been proposed [7]-[9], but these models mostly address fracture

66   media and do not estimate the evolution of the hydraulic property in porous rocks.

67   In this study, a new coupled THMC numerical model that incorporates the important process

68   of the pressure dissolution, as well as the free-face dissolution and precipitation, was developed,

69   and the validity of the model was examined by replicating the experimental measurements

70   obtained from Elias and Hajash (1992) [19]. Subsequently, the long-term evolution of the

71   permeability in porous rock was predicted under the expected stress and temperature conditions

72   where high-level radioactive wastes are disposed. In particular, the influence of the pressure

73   dissolution on the change in the rock permeability was examined intensively.

74   When any numerical model is developed, it may be dilemmatic to consider the balance

75   between the simplicity and the precision of the model. Complex models that incorporate a number

76   of equations to be solved may require time-consuming handling during pre- and post-processing,

77   and lengthy calculation time. Therefore, simpler or more straightforward numerical models with

78   satisfactory precision are preferred for general users. By focusing selectively on the geochemical

79   process of the pressure dissolution, the minor objective of this study is to develop a relatively

80   simple model.

81

82

2. Model description

84   The coupled THMC model developed in this work enables the change in permeability of

85   porous rocks to be followed with time by considering the interactions of the thermal, hydraulic,

86   mechanical, and geochemical processes (i.e., heat transfer, groundwater flow in saturated porous

87   media, stress/deformation, mass transport, and mineral dissolution/precipitation). The processes

88   considered in this model are schematically summarized in **Figure 1**. As is apparent from this

89   figure, the two-way interactions are taken into account between the T and H, the H and C, and the

90   C and T components. In the M component, the stress distribution is calculated and then rendered

91   to calculate a chemo-mechanical process, which is referred to as CM in **Figure 1**. In the C

92   components, two different chemical processes are incorporated into the model; one is the

93   free-surface dissolution/precipitation (CF) and the other is the pressure solution (CM). The

94   pressure solution includes three serial processes - mineral dissolution at the stressed contacts,

95   diffusive transport through the thin film of water, and re-precipitation of the mineral matter at the

96   pore wall. The mineral dissolution at the stressed contacts is explicitly integrated into the

97   proposed model as the CM component. It should be noted that we have proposed conceptual

98   chemo-mechanical models to predict the change in permeability of porous and fractured rocks

99   [20]-[24], and that this work is an attempt to fit the conceptual model into the coupled numerical

100   model and to conduct numerical simulations at a field scale instead of a representative element

101   scale. It should be also noted that the interactions between the H and M and the M ansd T

102   components are intentionally omitted in this work. These processes may influence the change in

103   permeability, but the main focus of the current work is to examine the effects of the geochemical

104   reactions (i.e., free-face dissolution/precipitation and pressure dissolution) on the change in

105   permeability by simplifying the developed model.

106

107   *2.1   Governing equations*

108   The equations used to model each of the THMC processes are presented in this section. In

109   this work, COMSOL Multiphysics [25] is utilized to solve the differential equations describing

110   the THMC processes. The calculation procedure is shown in **Figure 2** and the details are

111   described hereinafter. The coupled THMC processes are solved sequentially by exchanging the

112   dependent variables (i.e., porosity/permeability, flow velocity, stress, temperature, and

113   dissolution/precipitation rate constants).

114   The groundwater flow in saturated rocks is simply modeled by the conservation of water

115   mass and by assuming the Darcian flow, given by

116
$$\frac{\partial(\rho_w \phi)}{\partial t} + \nabla \cdot (\rho_w \boldsymbol{u}) = f_m ,$$
(1)

117
$$\boldsymbol{u} = -\frac{\boldsymbol{k}}{\mu}(\nabla p + \rho_w g \nabla D) ,$$
(2)

118 where ρ_w [kg m^{-3}] is the density of the fluid, ϕ [-] is the porosity, $\boldsymbol{u}$ [m s^{-1}] is the fluid velocity

119 tensor, f_m [kg m^{-3} s^{-1}] is the source term for the flow, $\boldsymbol{k}$ [m^2] is the rock permeability tensor, μ [Pa

120 s] is the fluid dynamic viscosity, p [Pa] is the fluid pressure, g [m s^{-2}] is the gravity acceleration,

121 and D [m] is the potential head. The temperature-dependent variables of ρ_w and μ are evaluated at

122 arbitrary temperatures within the calculation scheme [25].

123   The heat transfer is evaluated by considering thermal convection and conduction without the

124 radiation effect, as follows:

125
$$(\rho C_p)_{eq}\frac{\partial T}{\partial t} + \rho_w C_{p,w}\boldsymbol{u}\cdot\nabla T = \nabla\cdot(\boldsymbol{k}_{eq}\nabla T) + Q_h ,$$
(3)

126 where T [K] is the temperature, $(\rho C_p)_{eq}$ [J K^{-1} m^{-3}] is the equilibrium volumetric heat capacity,

127 $C_{p,w}$ [J kg^{-1} K^{-1}] is the heat capacity of the fluid, $\boldsymbol{k}_{eq}$ [W m^{-1} K^{-1}] is the equilibrium thermal

128 conductivity tensor, and Q_h [W m^{-3}] is the heat source. $(\rho C_p)_{eq}$ and $\boldsymbol{k}_{eq}$ can be obtained from the

129 following equations:

130
$$(\rho C_p)_{eq} = (1-\phi)\rho_m C_{p,m} + \phi\rho_w C_{p,w},$$
(4)

131
$$\boldsymbol{k}_{eq} = (1-\phi)\boldsymbol{k}_m + \phi\boldsymbol{k}_w ,$$
(5)

132 where ρ_m [kg m^{-3}] is the density of the solid, $C_{p,m}$ [J kg^{-1} K^{-1}] is the heat capacity of the solid, and

133 $\boldsymbol{k}_m$ and $\boldsymbol{k}_w$ [W m^{-1} K^{-1}] are the thermal conductivity tensors of the solid and the fluid, respectively.

134　　The numerical model enables the temperature-dependent variables of $C_{p,m}$, $C_{p,w}$, $\boldsymbol{k_m}$, and $\boldsymbol{k_w}$ to be

135　　followed at arbitrary temperatures [25].

136　　　　The mechanical process of the rock structure is evaluated by the quasi-static equilibrium

137　　equation and the typical Hooke's law, given by

138
$$-\nabla \cdot \boldsymbol{\sigma} = \boldsymbol{F}_v, \tag{6}$$

139
$$\boldsymbol{\sigma} = \boldsymbol{E} : \boldsymbol{\varepsilon} \ , \tag{7}$$

140　　where $\boldsymbol{\sigma}$ [Pa] is the stress tensor, $\boldsymbol{F}_v$ [Pa m^{-1}] is the body force, $\boldsymbol{E}$ [Pa] is the elasticity tensor, and $\boldsymbol{\varepsilon}$

141　　[-] is the strain tensor. In this work, the thermal stress and the inelastic behavior are disregarded

142　　for simplicity. A self-weight analysis is conducted to obtain the initial stress field, while the

143　　change in stress distribution by the cavity excavation is calculated using these equations.　.

144　　　　The advection-diffusion equation is used to calculate the solute transport behavior. The

145　　mechanical dispersion and the retardation due to the sorption processes are not considered here.

146
$$\frac{\partial (c_i \phi)}{\partial t} + \boldsymbol{u} \cdot \nabla c_i = \nabla \cdot (\phi \tau \boldsymbol{D}_{b,i} \nabla c_i) + R_i , \tag{8}$$

147　　where c_i [mol m^{-3}] is the concentration of solute i, τ [-] is the coefficient related to tortuosity, $\boldsymbol{D}_{b,i}$

148　　[m^2 s^{-1}] is the diffusion coefficient tensor, and R_i [mol m^{-3} s^{-1}] is the solute source or sink of solute

149　　i. The diffusion coefficient is controlled by the system temperature and can be defined by an

150　　Arrhenius-type equation [26], as

151
$$D_{b,i} = D_{b,i}^0 \exp(-E_{D,i}/RT),\qquad(9)$$

152 where $D_{b,i}^0$ [m^2 s^{-1}] and $E_{D,i}$ [J mol^{-1}] are the pre-exponential factor and the activation energy of

153 the diffusion of solute i, respectively, and R [J mol^{-1} K^{-1}] is the gas constant.

154   The source/sink term, R_i, is calculated by considering both free-face dissolution/precipitation

155 and pressure dissolution, and can be expressed by

156
$$R_i = R_i^{FF} + R_{diss,i}^{PS},\qquad(10)$$

157 where R_i^{FF} and $R_{diss,i}^{PS}$ [mol m^{-3} s^{-1}] are the rates of free-face dissolution/precipitation and

158 pressure dissolution, respectively. They are the physical quantities that describe the mineral

159 dissolution and precipitation per volume and time. The rate of the free-face

160 dissolution/precipitation is defined by [10]

161
$$R_i^{FF} = k_+ A\,(a_{H^+})^n (1 - Q/K),\qquad(11)$$

162 where k_+ [mol m^{-2} s^{-1}] is the mineral dissolution rate constant, A [m^2 m^{-3}] is the specific surface

163 area, a_{H^+} [-] is the activity of H^+, and n [-] is the constant, which may be obtained from

164 experimental observations in the literature. Q [-] is the ionic activity product and K [-] is the

165 equilibrium constant. When $Q/K <1$, free-face dissolution occurs; when $Q/K >1$, free-face

166 precipitation occurs. The specific surface area is obtained by the measurement using the BET

167 method, given as follows:

168
$$A = A_{BET}\,\rho_m,\qquad\qquad(12)$$

169 where A_{BET} [m^2 kg^{-1}] is the specific surface area determined by the BET method.

170   In this work, the rock is assumed to be composed purely of quartz, and subscript i in Eqs. (8)

171 - (10) is omitted hereinafter. The equilibrium and the dissolution rate constants in Eq. (11) are

172 obtained from PHREEQC [27] and Rimstidt and Barnes (1980) [28], respectively. These

173 constants are temperature-dependent and are given via polynomial approximation and by an

174 Arrhenious expression, as follows:

175
$$K = \sum_{m=0}^{7} \alpha_m T^m,\qquad\qquad(13)$$

176
$$k_+ = k_+^0 \exp(-E_{k_+}/RT),\qquad\qquad(14)$$

177 where α_m (m=0-7) [-] is the constant, k_+^0 [mol m^{-2} s^{-1}] is the pre-exponential factor, and E_{k+} [J

178 mol^{-1}] is the activation energy of the mineral dissolution.

179   Incorporating the process of pressure dissolution into the developed model is the most

180 important task in this work. As described above, we have developed conceptual models that

181 describe the process [20]-[24]. The flux that represents the pressure dissolution is driven by the

182 gradient in the chemical potential between the highly-stressed contacts and the less-stressed site

183 of the pore walls [13], [26]. Dissolution is most conveniently defined in terms of a dissolution

184 mass flux, $\dot{M}_{diss}^{PS}$, the rate of addition of dissolved mass into solution at the interface, given as

185 [20]

186
$$\dot{M}_{diss}^{PS} = \frac{3V_m^2(\sigma_a - \sigma_c)k_+\rho_g A_c}{RT},$$
(15)

187   where V_m is the molar volume of the solid (2.27×10^{-5} m^3 mol^{-1} for quartz), σ_a [Pa] is the

188   disjoining pressure [29] equal to the amount by which the pressure acting at the contacts exceeds

189   the hydrostatic pore pressure, ρ_g is the grain density (2650 kg m^{-3} for quartz), A_c [m^2] is the area

190   of the grain contact, and σ_c [Pa] is the critical stress, which defines the stress state where the

191   compaction of the grain aggregate will effectively halt [20]. This stress is determined by

192   considering the energy balance under applied stress and temperature conditions, given by [26],

193   [30]

194
$$\sigma_c = \frac{E_m(1 - T/T_m)}{4V_m},$$
(16)

195   where E_m and T_m are the heat and temperature of fusion, respectively ($E_m = 8.57$ kJ mol^{-1}, $T_m =$

196   1883 K for quartz).

197   Based on Eq. (15), the rate of the pressure dissolution, R_{diss}^{PS}, is derived through the following

198   procedure. Firstly, the strain rate due to the pressure dissolution is given as [20]

199
$$\dot{\varepsilon}_{diss}^{PS} = \frac{\dot{M}_{diss}^{PS}}{d\,\rho_g A_c} = \frac{3V_m^2 k_+}{RTd}\left(\frac{\sigma_{eff}}{R_c} - \sigma_c\right),$$
(17)

200
$$\sigma_a = \frac{\sigma_{eff}}{R_c},$$
(18)

201   where $\dot{\varepsilon}_{diss}^{PS}$ [-] is the strain state, d [m] is the grain diameter, σ_{eff} [Pa] is the effective stress

202   exerted in the representative element, and R_c ($0 < R_c < 1$) [-] is the contact-area ratio. In this work,

203   the FE analyses are conducted with 2-D meshes in the following sections. To this end, the

204   effective stress is replaced with the von Mises stress that can boil any complex stress conditions

205   down to a single representative scalar value. Therefore, Eq. (17) may be expressed as

$$\dot{\varepsilon}_{diss}^{PS} \approx \frac{3V_m^2 k_+}{RTd}\left(\frac{\sigma_{VM}}{R_c} - \sigma_c\right),$$ (19)

$$\sigma_{VM} = \sqrt{\frac{3}{2}\boldsymbol{\sigma}:\boldsymbol{\sigma}},$$ (20)

208   where σ_{VM} [Pa] is the von Mises stress. When the system is assumed to be simple cubic packing

209   with uniformly sized contacting spheres (**Figure 3**), the volumetric rate induced by the pressure

210   dissolution can be defined by

$$\dot{V}_{diss}^{PS} = \frac{\Delta d \cdot d^2}{\Delta t} = \dot{\varepsilon}_{diss}^{PS} d^3 = \frac{3V_m^2 k_+ d^2}{RT}\left(\frac{\sigma_{VM}}{R_c} - \sigma_c\right),$$ (21)

212   where $\dot{V}_{diss}^{PS}$ [m^3 s^{-1}] is the volumetric rate of the pressure dissolution. The dissolution rate, with

213   respect to the representative element, can be simply evaluated by dividing the volumetric rate by

214   the molar volume, as

$$\frac{\dot{V}_{diss}^{PS}}{V_m} = \frac{3V_m k_+ d^2}{RT}\left(\frac{\sigma_{VM}}{R_c} - \sigma_c\right).$$ (22)

216   The volume of the representative element (**Figure 3**) is d^3 [m^3], and the number of grains per unit

217   volume should be d^{-3} [m^{-3}]. Finally, the rate of pressure dissolution is defined by multiplying Eq.

218   (22) by d^{-3}, as follows:

219
$$R_{diss}^{PS} = \frac{3V_m k_+}{RTd}\left(\frac{\sigma_{VM}}{R_c} - \sigma_c\right). \tag{23}$$

220 As the pressure dissolution proceeds, contact-area ratio R_c increases and corresponding porosity ϕ

221 decreases. Therefore, the relation between R_c and ϕ should be obtained to solve Eq. (23) with time.

222 By considering the geometrical scheme (see **Figure 3** and more details in Appendix A), it is given

223 by

224
$$R_c = \frac{12}{\pi}(1-\phi) - 2. \tag{24}$$

225 Consequently, the rate of pressure dissolution is rearranged by substituting Eq. (24) into Eq. (23),

226 as follows:

227
$$R_{diss}^{PS} = \frac{3V_m k_+}{RTd}\left(\frac{\sigma_{VM}}{(12/\pi)(1-\phi)-2} - \sigma_c\right). \tag{25}$$

228

229 *2.2   Modification of porosity and related permeability*

230   In this work, the change in porosity is only induced by the free-face dissolution/precipitation

231 and the pressure dissolution. The porosity rates evaluated by the two geochemical processes are

232 defined by

233
$$\dot{\phi}^{FF} = V_m R^{FF}, \tag{26}$$

234
$$\dot{\phi}_{diss}^{PS} = -V_m R_{diss}^{PS}, \tag{27}$$

235 where $\dot{\phi}^{FF}$ and $\dot{\phi}_{diss}^{PS}$ [s^{-1}] are the porosity rates of the free-face dissolution/precipitation and the

14

236 pressure dissolution, respectively. Therefore, the porosity at an arbitrary time is evaluated using

237 Eqs. (26) and (27), given by

$$\phi = \phi_i + \int \dot{\phi}^{FF} dt + \int \dot{\phi}_{diss}^{PS} dt , \qquad (28)$$

239 where ϕ_t [-] is the initial porosity. Once the porosity is calculated, the related permeability is also

240 evaluated by the Kozeny-Carman equation [31], as

$$k = k_i \frac{(1-\phi_i)^2}{(1-\phi)^2} \left(\frac{\phi}{\phi_i} \right)^3 , \qquad (29)$$

242 where k and k_i [m^2] are the permeability at an arbitrary time and the initial permeability,

243 respectively.

244

245

246 **3. Model verification**

247 In the previous section, we proposed a coupled THMC model to describe the evolution of

248 porosity/permeability in porous media. In order to verify the proposed model, the model

249 predictions are compared with the laboratory experiments performed by Elias and Hajash (1992)

250 [19]. The compaction of quartz sand, with a mean grain diameter of 180-250 μm, has been

251 completed under the constant effective stresses of 69.0, 34.5, and 17.2 MPa at 150°C. The

252 changes in porosity and the silica concentrations in the pore fluid were measured over time to

253 examine the chemical and physical processes associated with the pressure solution [19]. In this

254 work, both the rates of porosity reduction and the evolving concentrations of silica in the pore

255 fluid were predicted. The parameters utilized in the calculations are summarized in **Table 1**.

256   In the predictions, the domain whose porosity initially starts with 0.35, equivalent to that of

257 the experiments [19], was set to be a square with side lengths of 0.01 m. The uniaxial confining

258 pressures of 69.0, 34.5, and 17.2 MPa and the temperature of 150°C were applied as the boundary

259 conditions and as the initial condition, respectively. The silica concentration within the domain

260 was initially fixed at the equilibrium concentration of quartz at 150°C, which was obtained by Eq.

261 (13), and was followed over time by considering the free-face dissolution/precipitation and/or the

262 pressure dissolution of quartz. All the boundaries were assumed to be thermally and hydraulically

263 the outflow boundaries. The initial contact-area ratio, R_{c0}, was evaluated by assuming the Herzian

264 contacts, given by

$$R_{c0} = \left(\frac{3\sigma_{eff}\,\pi\left(1-\nu\right)^2}{4E} \right)^{2/3}, \tag{30}$$

265

266 where σ_{eff} [Pa] is the effective stress (i.e., 69.0, 34.5, or 17.2 MPa), ν [-] is Poisson's ratio, and E

267 [Pa] is Young's modulus. When the pressure dissolution proceeds, the contact-area ratio increases.

268 The change is obtained using Eqs. (24), (26), and (27), as

$$R_c = R_{c0} + \int \dot{R}_c dt$$

$$= R_{c0} - \frac{12}{\pi} \int \dot{\phi} dt$$

269 $$= R_{c0} - \frac{12}{\pi} \int \left(\dot{\phi}^{FF} + \dot{\phi}_{diss}^{PS} \right) dt$$ (31)

$$= R_{c0} - \frac{12}{\pi} \left(\int V_m \cdot R^{FF} dt - \int V_m \cdot R_{diss}^{PS} dt \right)$$

270   After every time step, the new R_c was updated and used for calculating the rate of the pressure

271   dissolution, R_{diss}^{PS}, in the following time step (see **Figure 2**). Note that in these verification

272   predictions, R_{diss}^{PS} was evaluated over time with Eq. (23) instead of Eq. (25) because R_c can be

273   evaluated directly with Eq. (31). It should also be noted that the specific surface area in Eq. (11)

274   cannot be obtained from the literature [19]. Therefore, by introducing roughness factor f_r [32],

275   which is the ratio of the true (microscopic) surface area over the apparent (geometric) surface area,

276   the model predictions were conducted. The relation between specific surface area A and

277   roughness factor f_r is defined as follows:

278 $$A = f_r A_{geo},$$ (32)

279   where A_{geo} [m^2 m^{-3}] is the apparent specific surface area, which is simply given by the ratio of the

280   surface area of the spherical grain of diameter d over the volume, as

281 $$A_{geo} = \frac{\pi d^2}{\frac{\pi d^3}{6}} = \frac{6}{d}.$$ (33)

282   In the model predictions, three kinds of roughness factors, namely, 10, 20, and 80, were utilized.

283   The values are congruent with the magnitude indicated by Anbeek [1992] [33], who concluded

284   that it ranged from 2.5 to 11 for freshly created surfaces, and Sverdrup [1990] [34], who reported

285   that it varied between 1.5 and 71 for 28 silicate minerals.

286   Predictions of the porosity reduction rates and the silica concentration rates normalized by

287   the initial values are shown in **Figure 4** and **Figure 5**, respectively, together with the data

288   measured in the experiments. Surprisingly, all the predicted porosity reduction rates with time

289   closely match the experimental measurements (**Figure 4**). Note that changing the roughness factor

290   has little effect on the evolution of the porosity; and thus, the predictions with different roughness

291   factors are not shown in **Figure 4**. In contrast, the predicted silica concentrations are clearly

292   dependent on which roughness factors are applied (**Figure 5**). The utilization of higher roughness

293   factors results in the prediction of lower silica concentrations. The system in the pore fluid is

294   always oversaturated with silica because that is initially equivalent to the equilibrium

295   concentration, and the additional solute is supplied from the grain contacts via the pressure

296   dissolution. Therefore, the rates of precipitation are augmented by the higher roughness factors,

297   resulting in the lower silica concentrations. The predictions show some variations because of the

298   different roughness factors, but they follow the tendency observed in the experiments well (i.e.,

299   the abrupt increase after applying the pressures and the gradual decrease with time). Overall, a

300   comparison of the results of the porosity reduction and the evolving silica concentrations between

301   the predictions and the experimental measurements gives us confidence to use the developed

302   model to examine the long-term evolution of the porosity/permeability in porous media due to the

303   free-face dissolution/precipitation and the pressure dissolution, dependent on the applied pressure,

304   temperature, and flow conditions.

305

306

307   **4. Long-term predictions of permeability**

308   The developed model was applied to predict the long-term evolution of the permeability in

309   sedimentary rock near radioactive wastes within a simulated repository. It should be noted that

310   although we used actual data from related literature in the following predictions, we do not

311   anticipate any specific sites for high-level radioactive waste repositories.

312

313   *4.1 Modelling conditions*

314   The calculation domain, of the rock density of 1700 kg/m^3, was set to be a rectangle with

315   vertical and horizontal lengths of 700 and 12.2 m, respectively. The canisters of radioactive

316   wastes were virtually installed as a heat source by setting them laterally at a depth of 450 m [35].

317   The horizontal length of 12.2 m was chosen for the domain because it may be one-half of the

318   center-to-center spacing of each cavity, of the diameter 2.22 m [35] (**Figure 6**). The rock for the

319   calculations was assumed to have been fully-saturated with water and to have been composed

320   purely of quartz, with the initial porosity of 0.40 [36]. The hydraulic and thermal gradients were

321   set to be 1/1000 and 5°C/100 m, respectively [37]. The surface temperature was fixed at 15°C.

322   The initial silica concentrations within the domain were assumed to be the equilibrium values,

323   which were evaluated by Eq. (13). The change in pH was not considered and the initial value was

324   set at pH = 7.

325   In this work, the Excavation Distributed Zone (EDZ) was modeled explicitly with respect to

326   the rock permeability. The scientific and technical report, summarizing the HLW disposal

327   construction in Japan [38], indicates that the EDZ in both sedimentary and crystalline rocks may

328   range, in the radial direction, from the periphery of the excavated cavity to roughly 1 m. Therefore,

329   the range of 0.8 m was modeled as the EDZ in our calculations (**Figure 6**). The permeability in

330   the EDZ was increased by two orders of magnitude greater than the sound rock [35], [39]. Note

331   that the thermal and the mechanical properties in the EDZ were assumed to be equivalent to those

332   of sound rock, because those in the EDZ were ill-defined, and examining the changes in

333   permeability due to geochemical processes is the most significant task in this work. In the actual

334   calculations, the changes in the von Mises stresses, due to the excavation, were predicted by

335   conducting a self-weight analysis (**Figure 7**). The evolved von Mises stresses, greater around the

336   periphery of the cavity, as is apparent in **Figure 7**, are the driving-force for the pressure

337   dissolution (see Eq. (25)). The heat source from the radioactive wastes was modeled by applying

338 the temperatures at the periphery of the cavity as the boundary conditions. The applied

339 temperatures over time were obtained from the literature [38], as shown in **Figure 8**. The

340 prediction period was set at 10^4 years after the excavation. All the boundaries, excluding the

341 periphery of the cavity, were assumed to be thermally and hydraulically the outflow boundaries.

342 The parameters utilized in the calculations are summarized in **Table 2**.

343

344 *4.2 Prediction results*

345   In this work, the predictions were conducted for two different cases – one was done by

346 considering the full processes illustrated in **Figure 2**, and the other was done by excluding only

347 the pressure dissolution, in order to examine the effect of the pressure dissolution on the change in

348 permeability with time. The former and the latter cases are called the "PS" and the "no-PS"

349 conditions hereinafter. Calculations for the no-PS condition were performed by merely making

350 R_{diss}^{PS} in Eq. (25) zero at all the calculation steps.

351   The change in the temperature distribution with time, predicted under the PS condition, is

352 shown in **Figure 9**. The temperature in the EDZ increases with time; it increases to more than

353 80°C between 10^1 and 10^2 years. Subsequently, it decreases with time and reaches a steady

354 temperature (i.e., ~45°C) after 10^4 years. This tendency is quite similar to the change in Si

355 concentration with time (**Figure 10**), which is reasonable. As the equilibrium concentration of Si

356 is only controlled by the induced temperature, the changes over time should be similar. It should

357 be noted that the predicted changes in both temperature and the Si concentration with time, under

358 the no-PS condition, show no great difference from those under the PS condition. This is because

359 the concentrations in the whole system approach the equilibrium values in a relatively short

360 period, through free-face precipitation, when additional solute is supplied in the pore fluid due to

361 the pressure dissolution, and through free-face dissolution, when the system temperature and the

362 related equilibrium concentration increase. Consequently, the Si concentrations are equivalent to

363 the equilibrium values throughout most of the calculation period.

364   The changes in permeability with time under the no-PS and the PS conditions are compared

365 (**Figure 11** and **Figure 12**). Note that the permeability is normalized by the initial value. As is

366 apparent from the figures, it changes little with time under the no-PS condition, while it decreases

367 with time and the reduction appears after 10^2 years under the PS condition. Specifically, the

368 reduction is significant within the EDZ. This is because the pressure dissolution, resulting in

369 porosity reduction, is enhanced by the increase in the von Mises stress due to the cavity

370 excavation (see **Figure 7**), and an additional reduction in porosity is caused by the free-face

371 precipitation induced by the supply of the dissolved silica through the pressure dissolution. In

372 order to further investigate the influence of the pressure dissolution on the permeability change

373 within the EDZ, the changes with time at four specific locations, shown in **Figure 13**, are depicted

374   in **Figure 14**. Three of the four points are located within the EDZ, and the fourth one is 5 m away

375   from the periphery of the cavity. No change in permeability is observed under the no-PS condition.

376   In reality, the free-face precipitation of the secondary minerals, induced by the dissolution of the

377   cement materials, may cause changes in the porosity/permeability, but it is not the case in this

378   work. On the other hand, the permeability at No. 1 decreases by one order of magnitude in 10^4

379   years. However, the reduction is locally limited and is not observed at No. 4, which is located at

380   one-fourth of the center-to-center spacing of each cavity (**Figure 14**). In the current predications,

381   the decrease in permeability was observed only under the PS condition. This should result in the

382   delay of the transportation of radioactive materials, and the influence needs to be examined

383   quantitatively.

384   As a parametric study, predictions are made by varying the parameters of initial porosity ϕ_i

385   and critical stress σ_c, that should control the rate of the pressure dissolution (see Eq. (25)) to

386   examine the influence on the change in permeability. Two different initial porosities, 0.40 and

387   0.45, are selected to simulate Horonobe mudstone in Japan [36], and three levels of critical stress,

388   15, 50, and 80 MPa, are set for the analysis. The change in permeability at observation point No. 1,

389   shown in **Figure 13**, is shown in **Figure 15**. It is obvious that when a higher critical stress is

390   applied, less change in permeability is observed. This is because the effect of the pressure

391   dissolution becomes smaller when the difference between the von Mises stress and the critical

392   stress is smaller, as is clear from Eq. (25). In particular, at 80 MPa, the permeability hardly

393   changes in the case of $\phi_i = 0.40$, and it decreases roughly 30 % for 10^4 years in the case of 0.45.

394   From the above calculations, we have confirmed that choosing the right values for the critical

395   stress is of great importance to achieving precise predictions.

396

397

398   **5.   Conclusions**

399   A coupled THMC model was developed to investigate the long-term evolution of the

400   permeability in sedimentary rocks. The model solves the heat transfer, the groundwater flow, the

401   variation   in   induced   stresses,   and   the   geochemical   reactions   (i.e.,   the   free-face

402   dissolution/precipitation and the pressure dissolution), and their interactions. The changes in

403   porosity and silica concentration in the quartz aggregates were examined to test the adequacy of

404   the developed model in representing the experimentally observed behavior [19]. The predictions

405   showed an excellent agreement with the experimental observations. Subsequently, the verified

406   model was applied to examine the influence of the pressure dissolution on the evolution of the

407   permeability in sedimentary rocks where a radioactive waste repository may be constructed, in

408   considering the expected temperature, flow, and stress conditions. The predictions confirmed that

409   the process of the pressure dissolution decreased the permeability especially close to the

410 excavated cavity by one order of magnitude smaller than the initial value, which should delay the

411 transportation of the radioactive materials.

412   The developed model is straightforward and relatively simple because some interactions

413 among the THMC processes are omitted, but it enables the long-term evolution of the

414 permeability under arbitrary stress and temperature conditions to be followed over time with some

415 precision. Generally, when considering coupling processes for solving complicated nonlinear

416 problems, the uncertainty should be significant. Therefore, it is always important to ponder

417 whether complex, fully-coupled models are necessary for achieving sufficiently high precision. In

418 the near future, we will update the current model by taking into account the omitted processes

419 among the THMC interactions (e.g., the hydraulic-mechanical interactions; see **Figure 1**), and

420 examine whether or not the updates are indeed meaningful to the problems of interest.

421

422

428   in this work are available upon request from the authors.

429

430

APPENDIX A: Relation between contact-area ratio and porosity

432   Solid volume V_s, in the representative elementary volume, is obtained by subtracting the

433   sums of the volumes truncated between the contacts of two hemispheres from the volume of a

434   sphere of diameter d, given by

$$V_s = \frac{1}{6}\pi h(3a^2 + \frac{3d^2}{4} + h^2),$$
(A1)

436   where h is one-half of the domain height and a is the radius of the contact area. One-half of the

437   domain height, h, is given by

$$h = \sqrt{\frac{d^2}{4} - a^2}.$$
(A2)

439   The porosity, ϕ, is obtained by subtracting the solid volume, V_s, divided by the total volume of the

440   domain, V_t, from one, as follows:

$$\phi = 1 - \frac{V_s}{V_t} = 1 - \frac{\frac{1}{6}\pi\sqrt{\frac{d^2}{4} - a^2}(2a^2 + d^2)}{d^2\sqrt{\frac{d^2}{4} - a^2}} = 1 - \frac{\pi(2a^2 + d^2)}{6d^2}.$$
(A3)

442   The radius of the contact area is expressed by

$$a^2 = \frac{d^2}{4}R_c.$$
(A4)

444   By substituting Eq. (A3) into Eq. (A2), porosity ϕ is rearranged as

26

445

$$\phi = 1 - \frac{\pi \left(\frac{d^2}{2} R_c + d^2 \right)}{6d^2} = 1 - \left\{ \frac{\pi}{12} (R_c + 2) \right\}. \qquad \text{(A5)}$$

446

$$\Rightarrow R_c = \frac{12}{\pi} (1 - \phi) - 2 . \qquad \text{(A6)}$$

447

448

Nomenclature

449	**Nomenclature**	
450	A	specific surface area [m^2 m^{-3}]
451	A_{BET}	specific surface area determined by the BET method [m^2 kg^{-1}]
452	A_c	area of the grain contact [m^2]
453	A_{geo}	apparent specific surface area [m^2 m^{-3}]
454	a_{H+}	activity of H^+ [-]
455	C_i	concentration of the solute i [mol m^{-3}]
456	$C_{p,m}$	heat capacity of the solid [J kg^{-1} K^{-1}]
457	$C_{p,w}$	heat capacity of the fluid [J kg^{-1} K^{-1}]
458	D	potential head of the fluid [m]
459	$\boldsymbol{D_{b,i}}$	diffusion coefficient tensor [m^2 s^{-1}]
460	d	grain diameter [m]
461	$\boldsymbol{E}$	elasticity tensor [Pa]
462	$E_{D,i}$	activation energy of the diffusion of the solute i [J mol^{-1}]
463	E_{k+}	activation energy of the mineral dissolution [J mol^{-1}]
464	E_m	heat of fusion [kJ mol^{-1}]
465	$\boldsymbol{F_v}$	body force [Pa m^{-1}]
466	f_m	source term for flow [kg m^{-3} s^{-1}]
467	f_r	roughness factor [-]
468	g	gravity acceleration [m s^{-2}]
469	K	equilibrium constant [-]
470	$\boldsymbol{k}$	rock permeability tensor [m^2]
471	$\boldsymbol{k_{eq}}$	equilibrium thermal conductivity tensor [W m^{-1} K^{-1}]

472	$\boldsymbol{k_m}$	thermal conductivity tensor of the solid [W m^{-1} K^{-1}]
473	$\boldsymbol{k_w}$	thermal conductivity tensor of the fluid [W m^{-1} K^{-1}]
474	k_+	dissolution rate constant [mol m^{-2} s^{-1}]
475	$\dot{M}_{diss}^{PS}$	rate of addition of dissolved mass into solution at the interface [kg s^{-1}]
476	p	fluid pressure [Pa]
477	Q	ionic activity product [-]
478	Q_h	heat source [W m^{-3}]
479	R	gas constant [J mol^{-1} K^{-1}]
480	R_c	contact-area ratio [-]
481	R_i^{FF}	rate of free-face dissolution/precipitation of the solute i [mol m^{-3} s^{-1}]
482	$R_{diss,i}^{PS}$	rate of pressure dissolution of the solute i [mol m^{-3} s^{-1}]
483	R_i	solute source or sink of the solute i [mol m^{-3} s^{-1}]
484	T	system temperature [K]
485	T_m	temperature of fusion [K]
486	$\boldsymbol{u}$	fluid velocity tensor [m s^{-1}]
487	$\dot{V}_{diss}^{PS}$	volumetric rate of the pressure dissolution [m^3 s^{-1}]
488	V_m	molar volume [m^3 mol^{-1}]
489	V_s	solid volume [m^3]
490		
491	*Greek letters*	
492	$\boldsymbol{\varepsilon}$	strain tensor [-]
493	$\dot{\varepsilon}_{diss}^{PS}$	strain rate due to the pressure dissolution [s^{-1}]

494	ϕ	porosity [-]
495	$\dot{\phi}^{FF}$	porosity rate of the free-face dissolution/precipitation [s^{-1}]
496	$\dot{\phi}_{diss}^{PS}$	porosity rate of the pressure dissolution [s^{-1}]
497	μ	dynamic viscosity of the fluid [Pa s]
498	ν	Poisson's ratio [-]
499	ρ_g	grain density [kg m^{-3}]
500	ρ_m	density of the solid [kg m^{-3}]
501	ρ_w	density of the fluid [kg m^{-3}]
502	$(\rho C_p)_{eq}$	equilibrium volumetric heat capacity [J K^{-1} m^{-3}]
503	$\boldsymbol{\sigma}$	stress tensor [Pa]
504	σ_a	stress acting at the contact area [Pa]
505	σ_c	critical stress [Pa]
506	σ_{eff}	effective stress [Pa]
507	σ_{VM}	von Mises stress [Pa]
508	τ	tortuosity [-]
509		

6. References

510

511 [1] Tsang CF (ed.). Coupled Processes Associated with Nuclear Waste Repositories. Elsevier

512 2012; ISBN 9780323142403: 816 pp.

513 [2] Tsang Y. Effects of coupled processes on a proposed high-level radioactive waste repository

514 at Yucca Mountain, Nevada. Geological Society of America Memoirs 2012; 209:363-393.

515 [3] Zheng L, Samper J. A coupled THMC model of FEBEX mock-up test. Phys Chem Earth

516 2008; 33:S486‑S498.

517 [4] Taron J, Elsworth D, Min K-B. Numerical simulation of

518 thermal-hydrologic-mechanical-chemical processes in deformable, fractured porous media.

519 Int J Rock Mech Min Sci 2009; 46:842-854.

520 [5] Nasir O, Fall M, Evgin E. A simulator for modeling of porosity and permeability changes in

521 near field sedimentary host rocks for nuclear waste under climate change influences.

522 Tunnelling Underground Space Technol 2014; 42:122-135.

523 [6] Kim J, Sonnenthal E, Rutqvist J. A sequential implicit algorithm of

524 chemo-thermo-poro-mechanics for fractured geothermal reservoirs. Comput Geotech 2015;

525 76:59-71.

526 [7] Lang PS, Paluszny A, Zimmerman RW. Hydraulic sealing due to pressure solution contact

527 zone growth in siliciclastic rock fractures. J Geophys Res 2015; 120:4080‑

528   4101,doi:10.1002/2015JB011968.

529   [8] McDermott C, Bond A, Harris, AF, Chittenden N, Thatcher K. Application of hybrid

530   numerical and analytical solutions for the simulation of coupled thermal, hydraulic,

531   mechanical and chemical processes during fluid flow through a fractured rock. Environ Earth

532   Sci 2015; DOI 10.1007/s12665-015-4422-7.

533   [9] Taron J, Elsworth D. Coupled mechanical and chemical processes in engineered geothermal

534   reservoirs with dynamic permeability. Int J Rock Mech Min Sci 2010; 47:1339-1348.

535   [10] Lasaga AC. Chemical Kinetics of Water-Rock Interactions. J Geophys Res 1984;89:

536   4009-4025.

537   [11] Croizé D, Renard F, Bjørlykke K, Dysthe DK. Experimental calcite dissolution under stress:

538   evolution of grain contact microstructure during pressure solution creep. J Geophys Res

539   2010; 115, B09207, doi:10.1029/2010JB000869.

540   [12] Neveux L, Grgic D, Carpentier C, Pironon J, Truche L, Girard JP. Experimental simulation

541   of chemomechanical processes during deep burial diagenesis of carbonate rocks. J Geophys

542   Res 2014; 119, 984.1007, doi:10.1002/2013JB010516.

543   [13] Raj R. Creep in polycrystalline aggregates by matter transport though a liquid phase. J

544   Geophys Res 1982; 87:4731-4739.

545   [14] Robin P-Y F. Pressure solution at grain to grain contacts. Geochim Cosmochim Acta 1978;

546   42:1383-1389.

547 [15] Spiers CJ, De Meer S, Niemeijer AR, Zhang X. Kinetics of Rock Deformation by Pressure

548   Solution and the Role of Thin Aqueous Films. In: Frontiers Science Series 2003:129e158.

549 [16] Weyl PK. Pressure solution and force of crystallization-A phenomenological theory. J

550   Geophys Res 1959; 64:2001-2025.

551 [17] Zhang X, Spiers CJ, Peach CJ. Compaction creep of wet granular calcite by pressure

552   solution at 28 C to 150 C. J Geophys Res 2010; 115 (B9):B09217.

553 [18] Zubtsov S, Renard F, Gratier JP, Guiguet R, Dysthe DK, Traskine V. Experimental pressure

554   solution compaction of synthetic halite/calcite aggregates. Tectonophysics 2004; 385:45-57.

555 [19] Elias BP, Hajash A. Change in quartz solubility and porosity change due to effective stress:

556   An experimental investigation of pressure solution. Geology 1982; 20:451-454.

557 [20] Yasuhara H, Elsworth D, Polak A. A mechanistic model for compaction of granular

558   aggregates moderated by pressure solution. J Geophys Res 2003; 108(11):2530,

559   doi:10.1029/2003JB002536.

560 [21] Yasuhara H, Elsworth D, Polak A. Evolution of permeability in a natural fracture: The

561   significant role of pressure solution. J Geophys Res 2004; 109(B3):B03204,

562   doi:10.1029/2003JB002663.

563 [22] Yasuhara H, Elsworth D, Polak A, Liu J, Grader A, Halleck P. Spontaneous Permeability

564   Switching in Fractures in Carbonate: Lumped Parameter Representation of Mechanically-

565   and Chemically-Mediated Dissolution. Transp Porous Media 2006; 65:385-409.

566   [23] Yasuhara H, Elsworth D. Compaction of a rock fracture moderated by competing roles of

567   stress corrosion and pressure solution. Pure Appl. Geophys 2008; 165:1289-1306.

568   [24] Yasuhara H, Kinoshita N, Ohfuji H, Lee DS, Nakashima S, Kishida K. Temporal alteration

569   of fracture permeability in granite under hydrothermal conditions and its interpretation by

570   coupled chemo-mechanical model. Appl Geochem 2011; 26:2074-2088.

571   [25] COMSOL2014 : COMSOL MULTIPHYSICS. Version 5.0, Available from

572   www.comsol.com.

573   [26] Revil A. Pervasive pressure-solution transfer: a poro-visco-plastic model. Geophys Res Lett

574   1999; 26:255-258.

575   [27] Parkhurst DL, Appelo CAJ. Description of Input and Examples for PHREEQC Version 3-A

576   Computer Program for Speciation, Batch-Reaction, One-Dimensional Transport, and Inverse

577   Geochemical Calculations, Online version available from

578   http://wwwbrr.cr.usgs.gov/projects/GWC_coupled/phreeqc/phreeqc3-html/phreeqc3.htm.

579   [28] Rimstidt JD, Barnes HL. The kinetics of silica-water reactions. Geochim Cosmochim Acta

580   1980; 44:1683-1699.

581   [29] Heidug WK. Intergranular solid-fluid phase transformations under stress: The effect of

582   surface forces. J Geophys Res 1995; 100:5931-5940.

583   [30] Stephenson LP, Plumley WJ, Palciauskas VV. A model for sandstone compaction by grain

584   interpenetration. J Sediment Petrol 1992; 62:11-22.

585   [31] Bear J. Dynamics of Fluids in Porous Media. Dover Publications Inc. 1972:166.

586   [32] Murphy WM, Helgeson HC. Thermodynamic and kinetic constraints on reaction rates

587   among minerals and aqueous solutions. IV. Retrieval of rate constants and activation

588   parameters for the hydrolysis of pyroxene, wollastonite, olivine, andalusite, quartz, and

589   nepheline. Am J Sci 1989; 289:17-101.

590   [33] Anbeek C. Surface roughness of minerals and implications for dissolution studies. Geochim

591   Cosmochim Acta 1992; 56:1461-1469.

592   [34] Sverdrup H. The Kinetics of Base Cation Release Due to Chemical Weathering. Lund

593   University Press, Lund, Sweden 1990:245pp.

594   [35] Suzuki H, Nakama S, Fujita T, Imai H, Sazarshi M. A long-term THMC assessment on the

595   geochemical behavior of the bentonite buffer. J Nucl Fuel Cycle Environ 2012; 19:39-50.

596   [36] Miyazawa D, Sanada H, Kiyama T, Sugita Y, Ishijima Y. Poroelastic coefficients for

597   siliceous rocks distributed in the Horonobe area, Hokkaido, Japan. J MMIJ 2011;

598   127:132-138.

599   [37] Kamei G, Honda A, Mihara M, Oda C, Murakami H, Masuda K, Yamaguchi K, Matsuda S,

600 Ichige S, Takahashi K, Meguro Y, Yamaguchi H, Sakakibara T, Sasaki T. Research and

601 development for treatment and disposal technologies of TRU waste JFY 2007 annual report.

602 JAEA-research 2008-082:1-84.

603 [38] Japan Nuclear Cycle Development Institute, 2000. Second Progress Report on Research and

604 Development for the Geological Disposal of HLW in Japan, Supporting Report 2 Repository

605 Design and Engineering Technology, H12: Project to Establish the Scientific and Technical

606 Basis for HLW Disposal in Japan. JNC TN1410 2000-003, IV-139-IV-160.

607 [39] Minato K (ed.). JAEA R&D review 2013; ISSN 2188-1456.

608

609

610   List of Tables

611

612   Table 1. Calculation parameters to simulate experimental results.

613   Table 2. Calculation parameters to simulate long-term permeability.

614

615

616

Table 1. Calculation parameters to simulate experimental results.

Diameter d [μm]	Temperature T [°C]	Effective stress σ_{eff} [MPa]	Critical stress σ_c [MPa]	Equilibrium constant K [mol m^{-3}]
215	150	69.0, 34.5, 17.2	73.2	1.79
Diffusion coefficient D_b [m^{2}s^{-1}]	Dissolution rate constant k_+ [mol m^{-2} s^{-1}]	Young's modulus E [GPa]		Poisson's ratio ν [-]
1.12×10^{-9}	2.51×10^{-9}	72.4		0.17

617

618

619

Table 2. Calculation parameters to simulate long-term permeability.

Rock type	Initial permeability k_i [m^2]	Young's modulus E [GPa]	Poisson's ratio ν [-]	Initial porosity ϕ_i [-]	Thermal conductivity k_{eq} [W m^{-1} K^{-1}]	Heat capacity C_p [J kg^{-1} K^{-1}]
EDZ	1.0×10^{-13}	2.5	0.30	0.40	1.60	1500
Sound	1.0×10^{-15}	2.5	0.30	0.40	1.60	1500

620

621

622   List of Figures

623

640   periphery of the cavity [38].

641   Figure 9. Change in temperature distribution with time in the range of 100 to 104 years under the

642   PS condition.

643   Figure 10. Change in Si concentration distribution with time in the range of 100 to 104 years

644   under the PS condition.

645   Figure 11. Change in normalized permeability with time in the range of 100 to 104 years under

646   the no-PS condition. No permeability change is confirmed.

647   Figure 12. Change in normalized permeability with time in the range of 100 to 104 years under

648   the PS condition. The permeability decreases with time. The reduction is especially significant

649   around the periphery of the cavity.

650   Figure 13. Specific locations where changes in permeability with time are observed.

651   Figure 14. The permeability changes with time at specific locations indicated in Figure 13((a) the

652   no PS condition and (b) the PS condition).

653   Figure 15. The permeability changes with time under the PS condition at No. 1, indicated in

654   Figure 13((a) initial porosity of 0.40 and (b) 0.45).

655

656

657
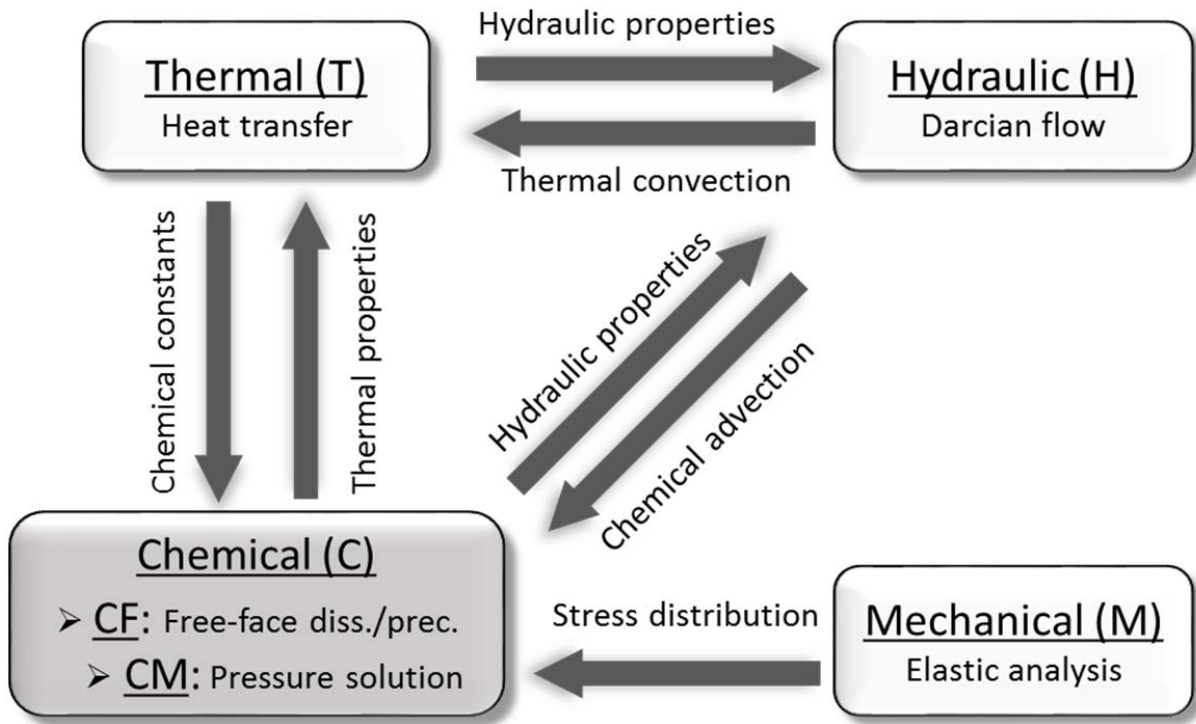
Figure 1. THMC interactions considered in the developed numerical model.

659

660
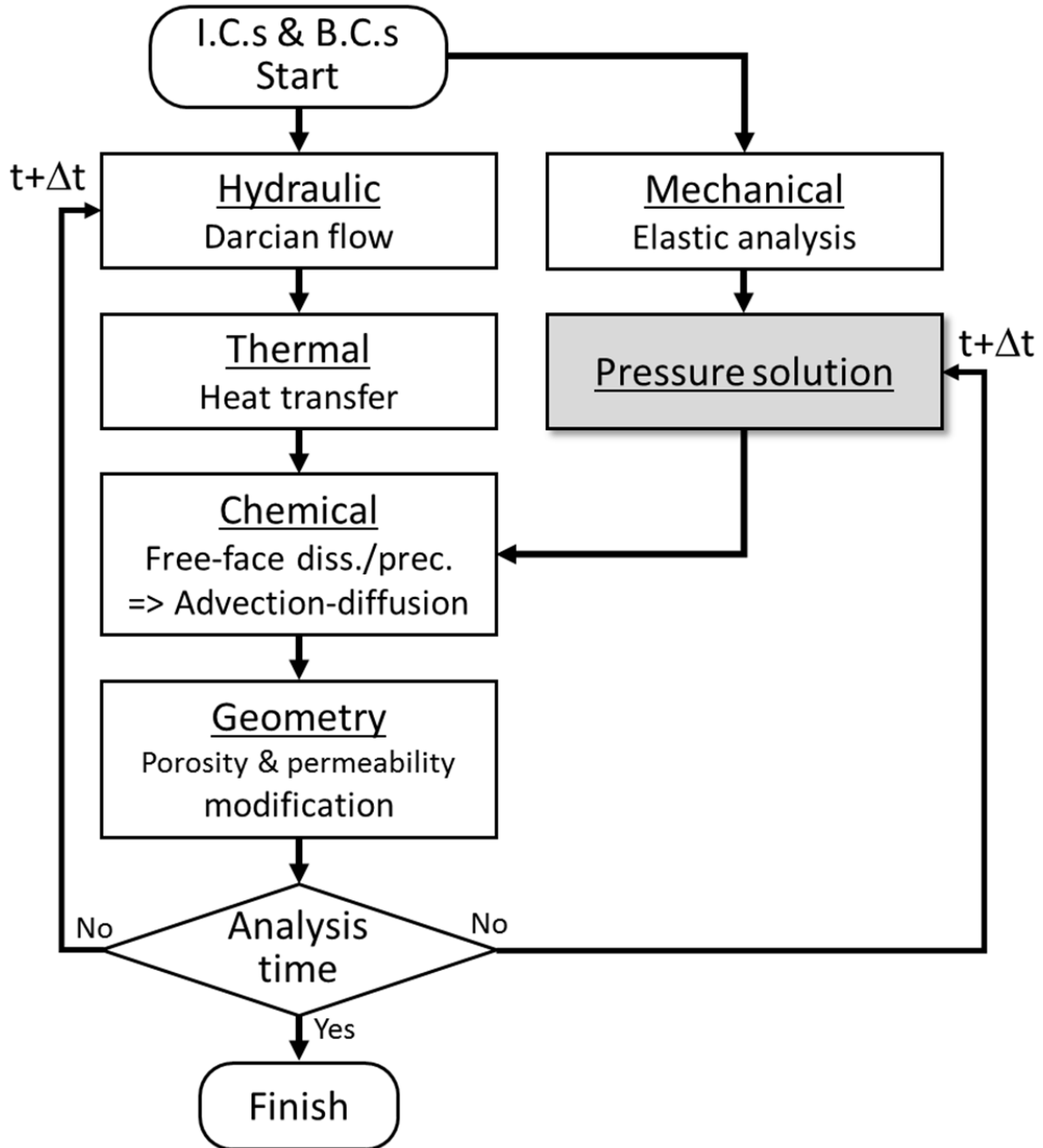
661

662   Figure 2. Sequential procedure to conduct consistent calculations of porosity change with time.

663
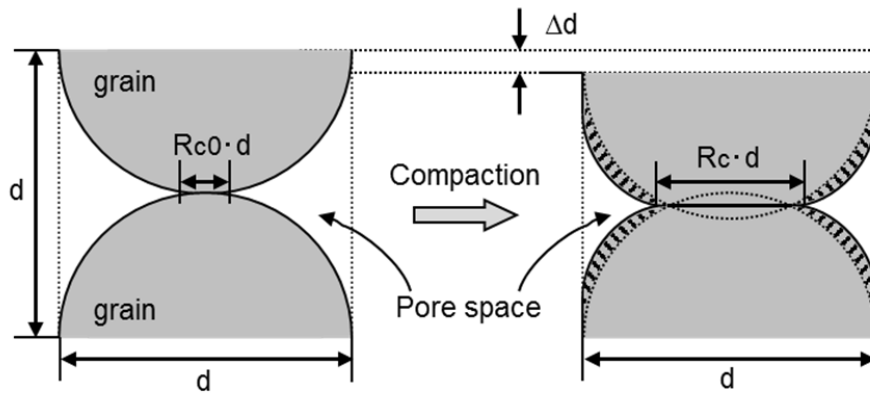
664

665 Figure 3. Geometrical model of grain-to-grain contact. Initially, two grains contact each other

666 with an initial contact-area ratio of R_{c0}. As compaction proceeds due to the pressure solution,

667 contact-area ratio R_c increases and free-face dissolution/precipitation occurs simultaneously,

668 resulting in porosity modification.

669

670

671

672
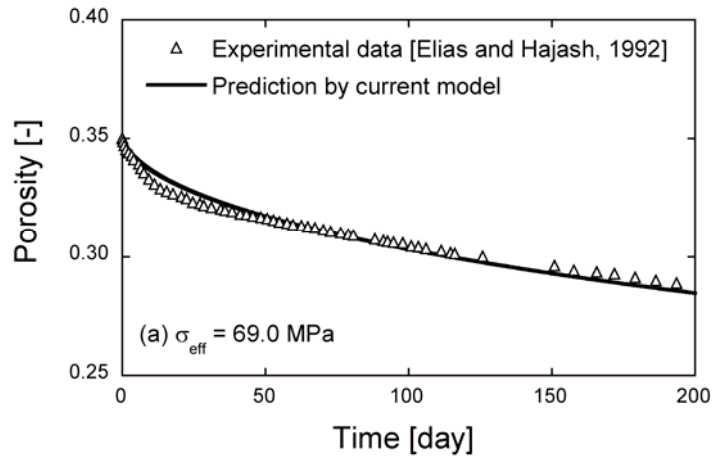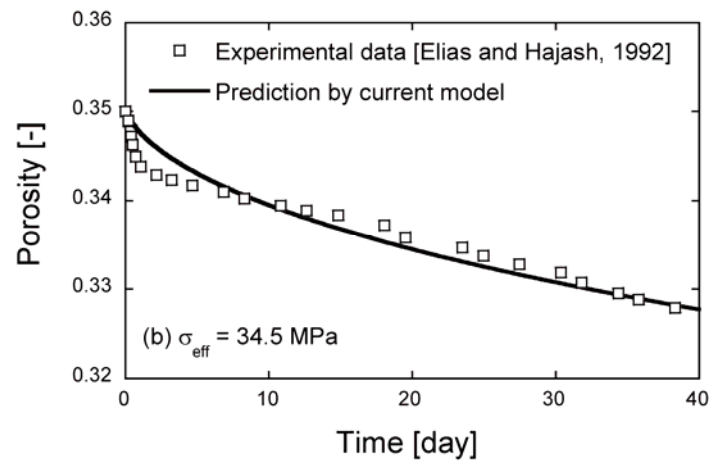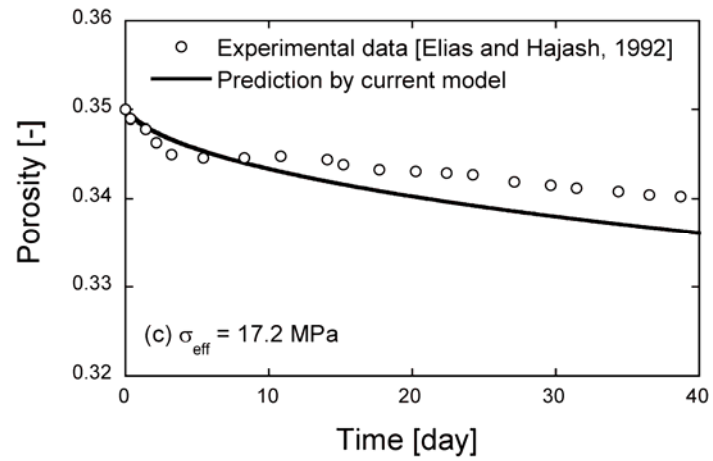
Figure 4. Comparison of porosity reduction with time between experimental data [19] and

674   predictions of the model.

675
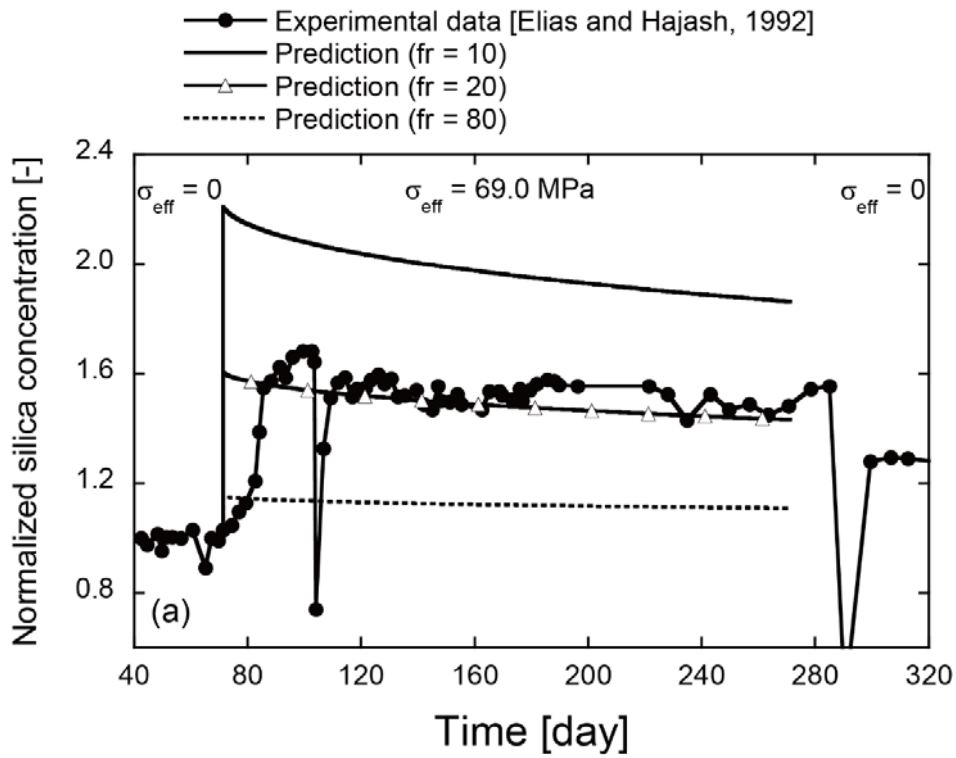
676
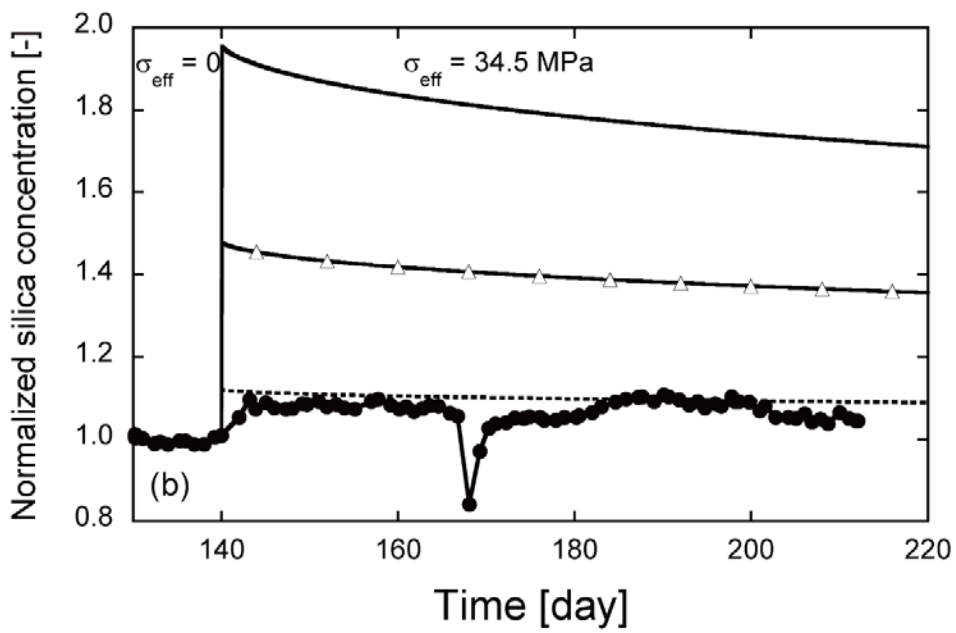
677

678 Figure 5. Comparison of silica concentration in pore fluid between experimental data [19] and

679 predictions of the model.

680
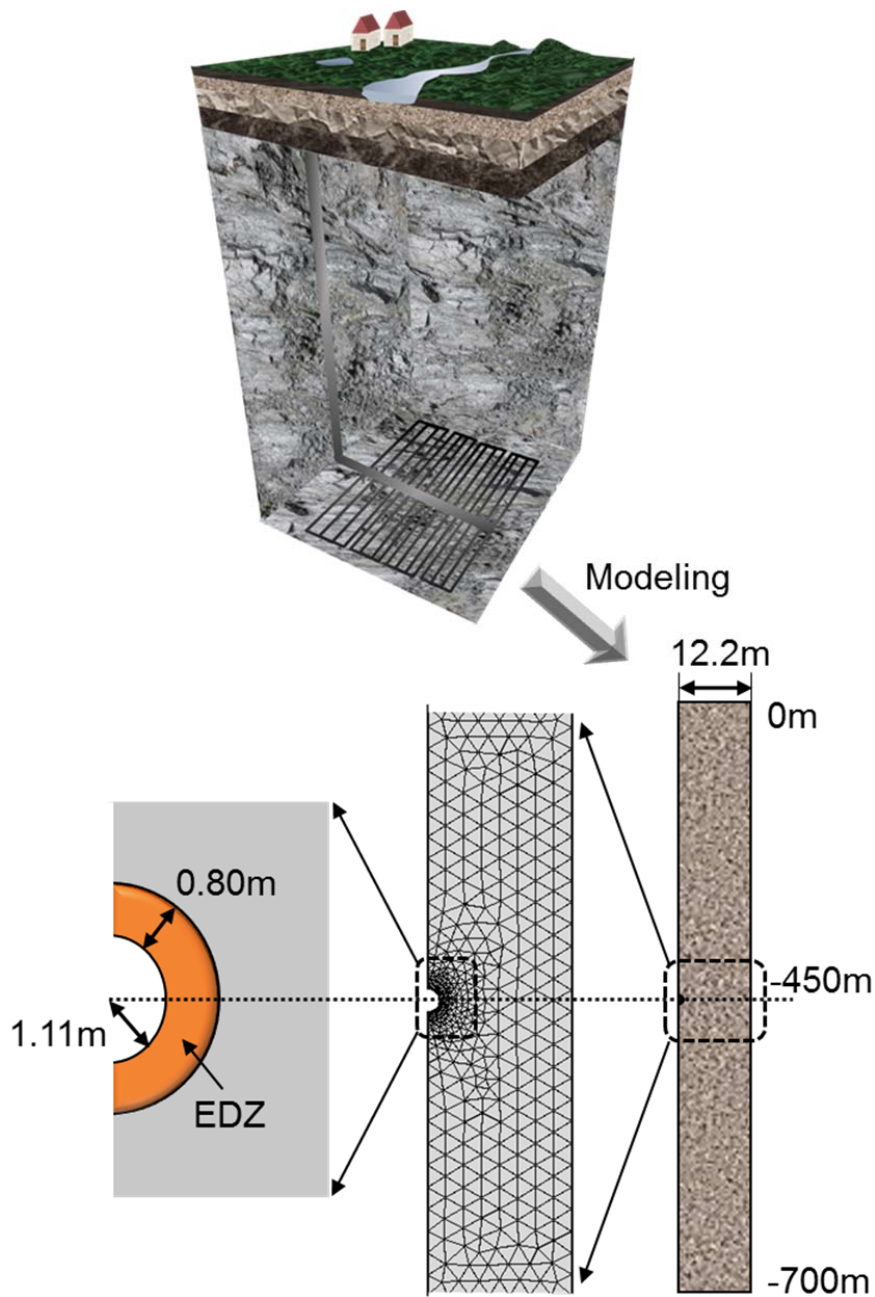
681

682   Figure 6. Calculation domain. The calculation domain is a rectangle with vertical and horizontal

683   lengths of 700 and 12.2 m, respectively. The cavity, with a diameter of 2.22 m, is excavated by

684   lateral setting at a depth of 450 m. The EDZ ranges, in the radial direction, from the cavity wall to

685   0.8 m.

686
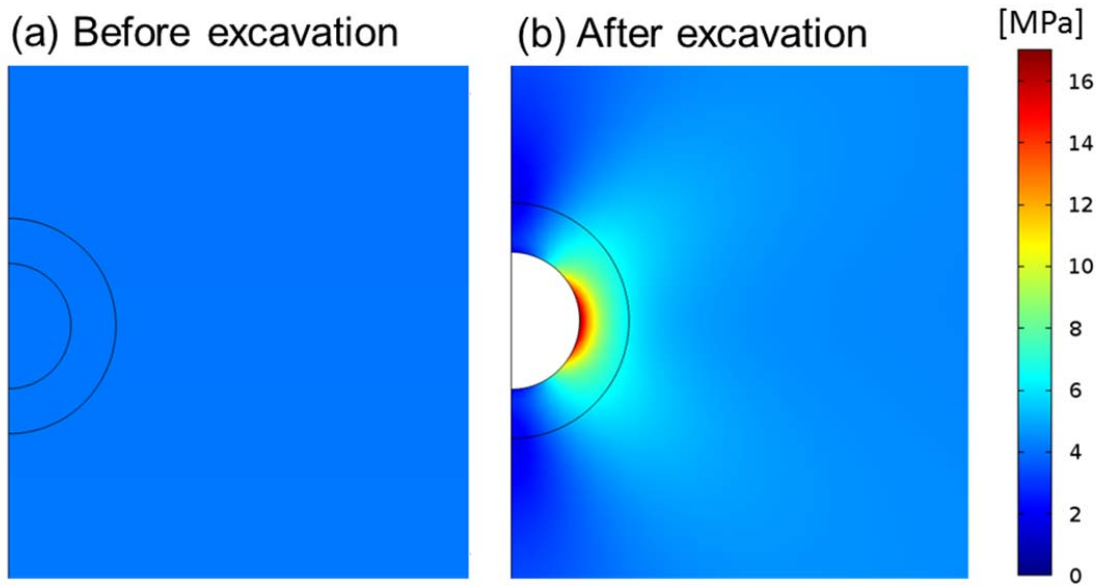
Figure 7. Distribution of von Mises stress before and after cavity excavation.

687

688

689

690

691

692
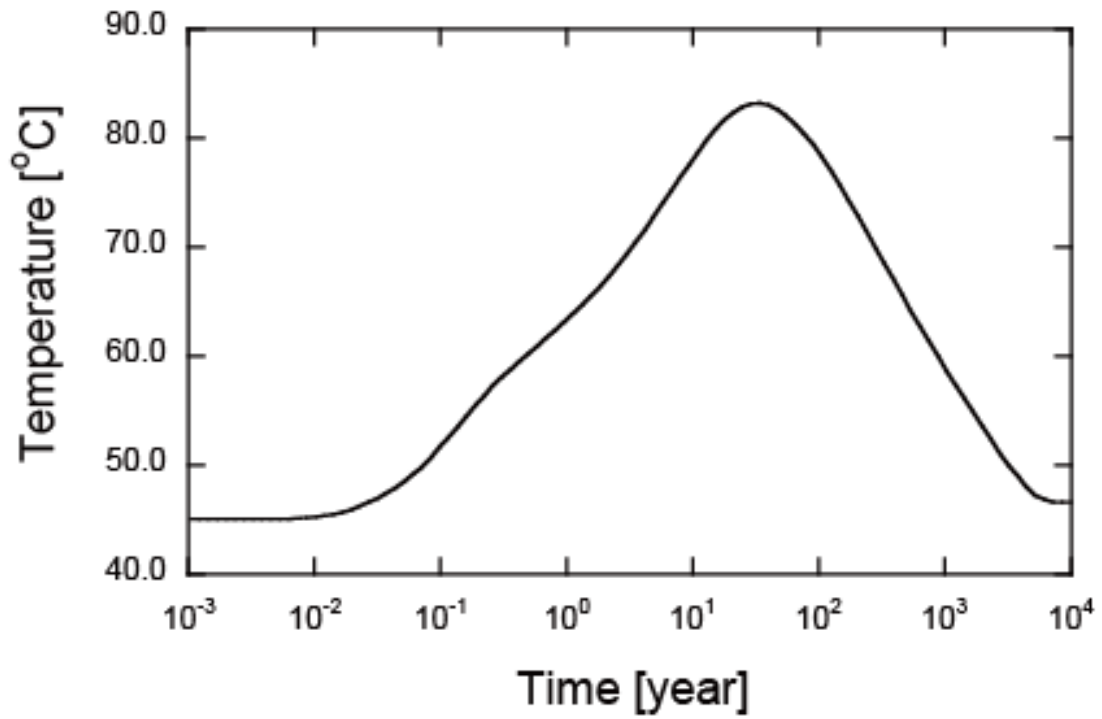
Figure 8. Temperature change with time that is used as the boundary condition applied on the

periphery of the cavity [38].

695

696

697
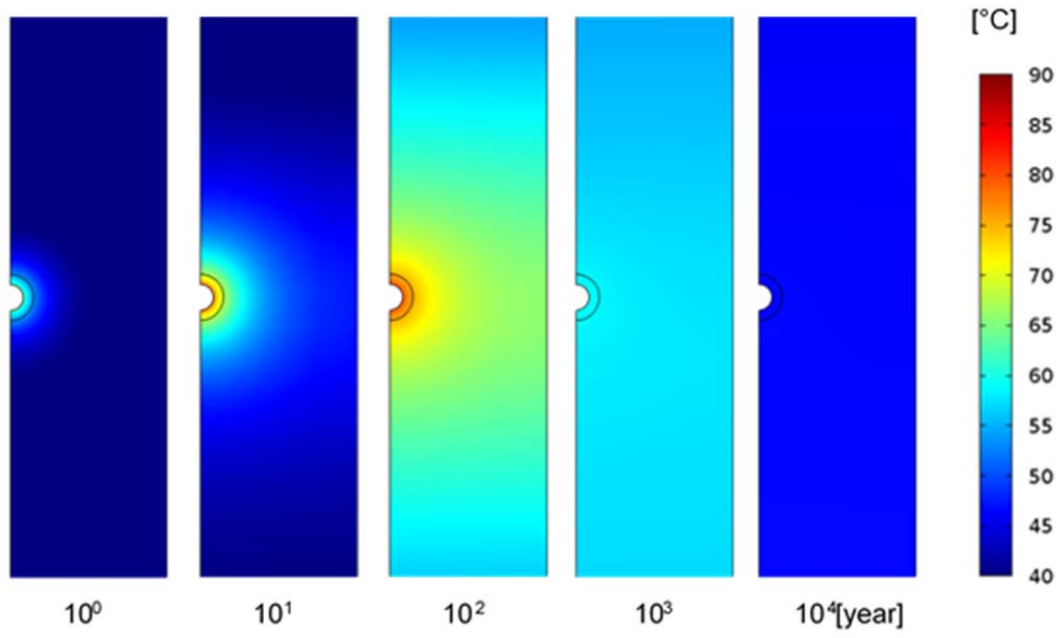
698

699   Figure 9. Change in temperature distribution with time in the range of 10^0 to 10^4 years under the

700   PS condition.

701
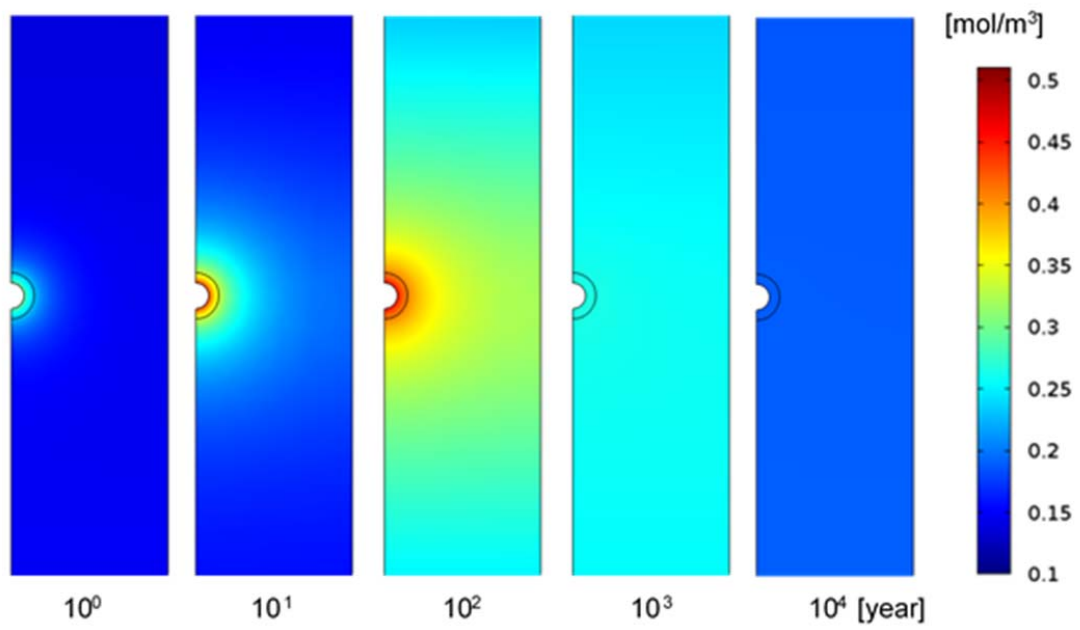
Figure 10. Change in Si concentration distribution with time in the range of 10^0 to 10^4 years under the PS condition.

707
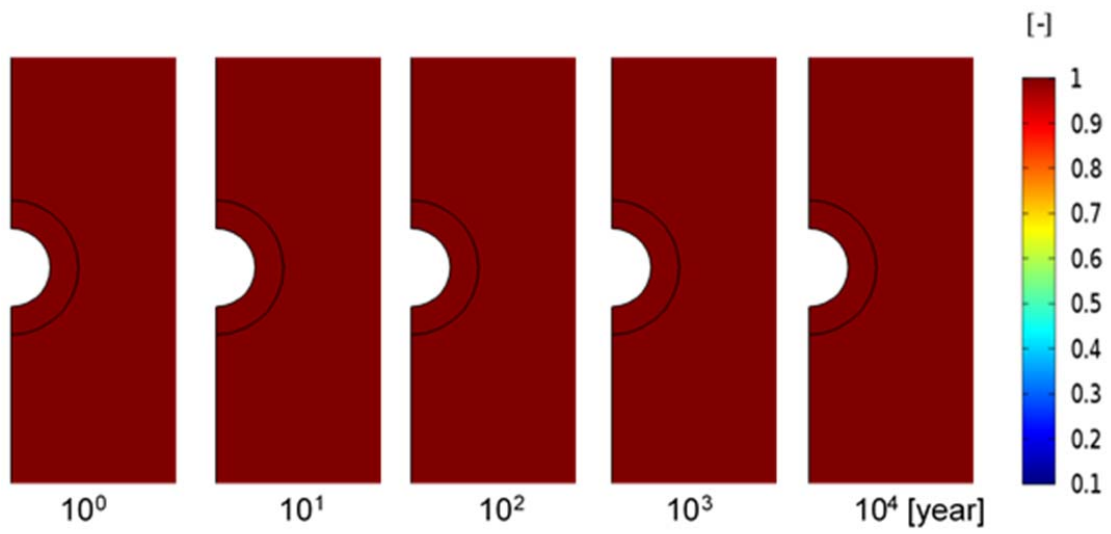
Figure 11. Change in normalized permeability with time in the range of 10^0 to 10^4 years under the

no-PS condition. No permeability change is confirmed.

710

711
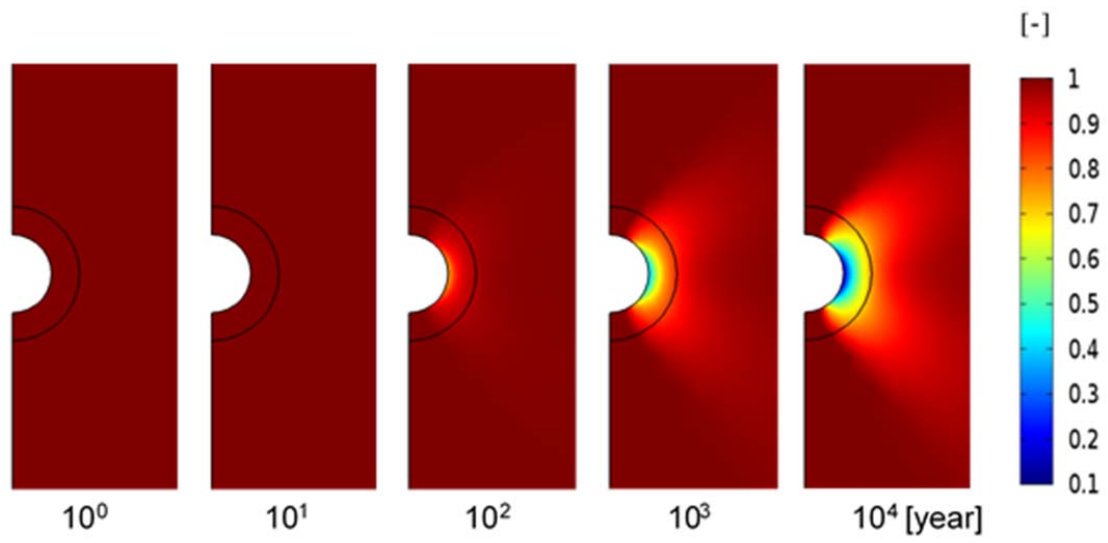
Figure 12. Change in normalized permeability with time in the range of 10^0 to 10^4 years under the

PS condition. The permeability decreases with time. The reduction is especially significant around

the periphery of the cavity.
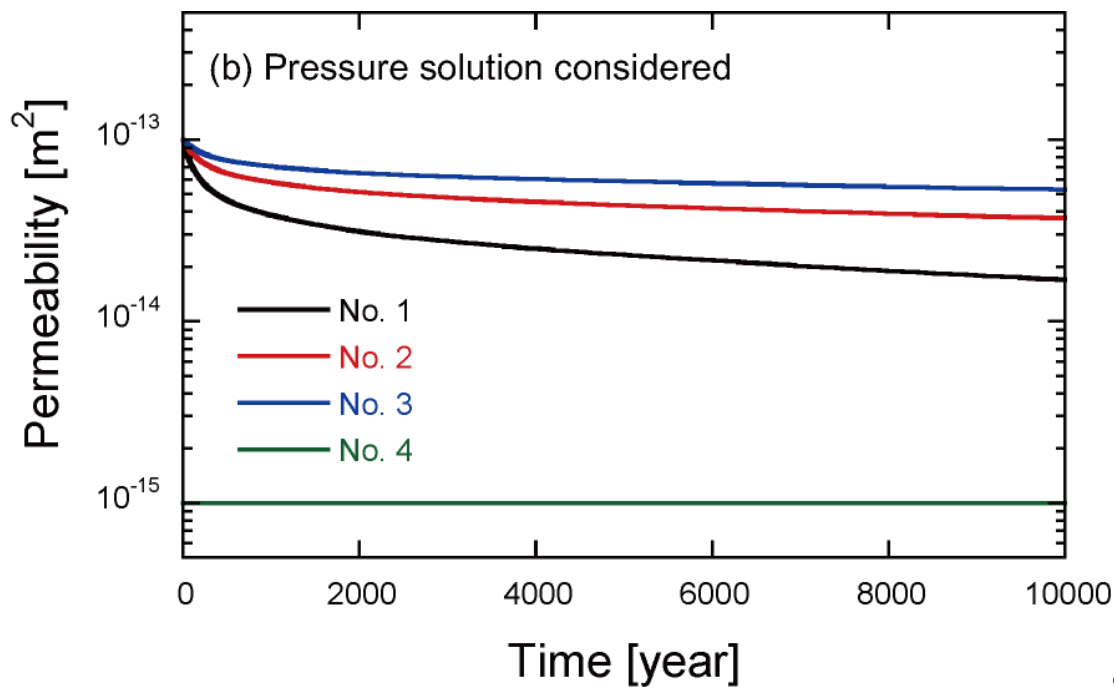
716
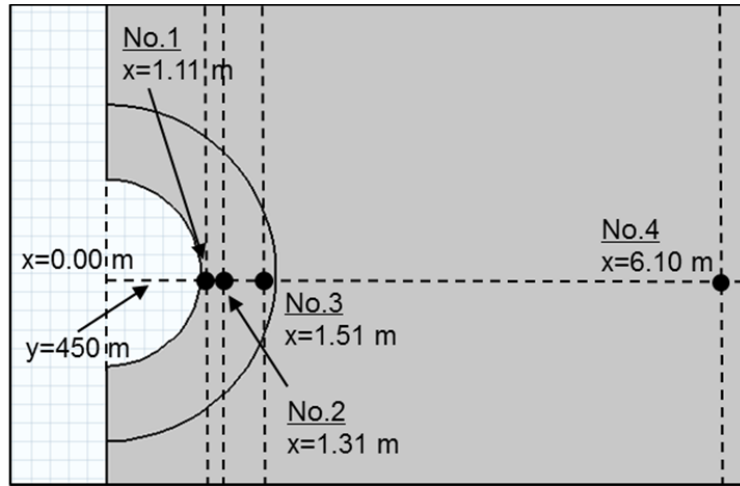
717

718   Figure 13. Specific locations where changes in permeability with time are observed.

719

720

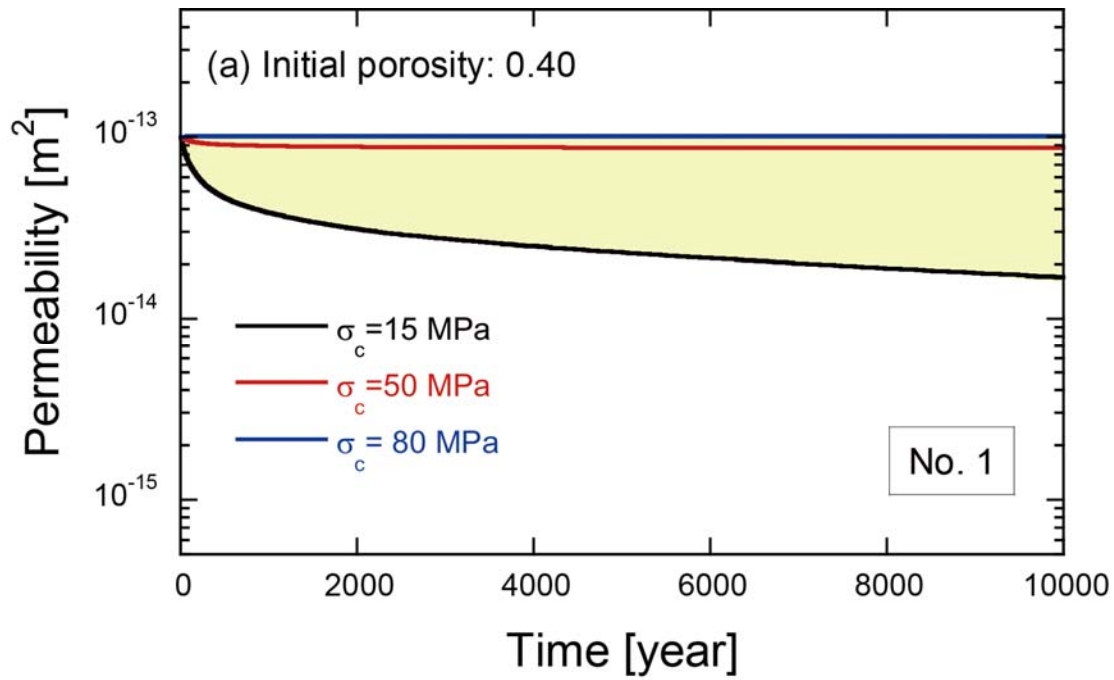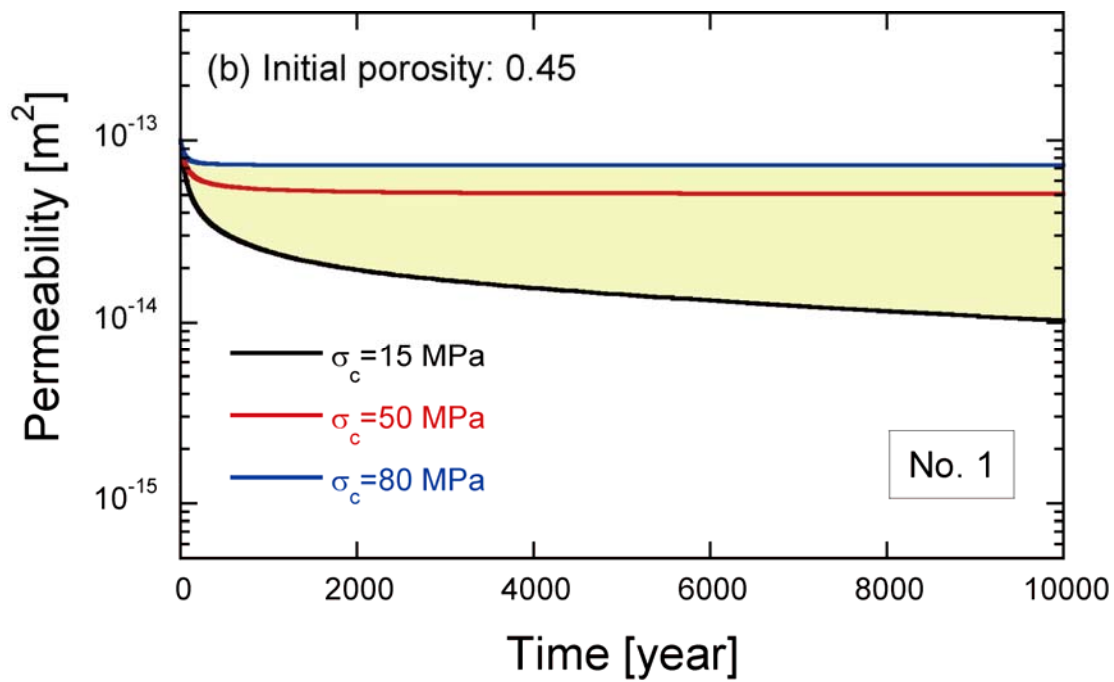721   9

Figure 14. The permeability changes with time at specific locations indicated in Figure 13((a) the

no PS condition and (b) the PS condition).

725

726

Figure 15. The permeability changes with time under the PS condition at No. 1, indicated in

Figure 13((a) initial porosity of 0.40 and (b) 0.45).

729